

**Weierstraß-Institut**  
**für Angewandte Analysis und Stochastik**  
**Leibniz-Institut im Forschungsverbund Berlin e. V.**

Preprint

ISSN 0946 – 8633

**Eigensolutions of the Wigner–Eisenbud problem for a  
cylindrical nanowire within finite volume method**

Paul N. Racec<sup>1,2</sup>, Stanley Schade<sup>3</sup>, Hans-Christoph Kaiser<sup>1</sup>

submitted: May 31, 2012

<sup>1</sup> Weierstrass Institute  
Mohrenstr. 39  
10117 Berlin  
Germany  
E-Mail: paul.racec@wias-berlin.de

<sup>2</sup> National Institute of Materials Physics  
PO Box MG-7  
077125 Bucharest Magurele  
Romania

<sup>3</sup> Brandenburg University of Technology Cottbus  
Faculty 1  
Postfach 101344  
03013 Cottbus  
Germany

No. 1709  
Berlin 2012



---

2010 *Mathematics Subject Classification.* 65N30, 65Z05, 35P99.

2010 *Physics and Astronomy Classification Scheme.* 62.23.Hj, 73.63.-b, 71.15.-m.

*Key words and phrases.* Finite element method, Schrödinger operator, cylindrical coordinates, R-matrix formalism, Wigner–Eisenbud problem, nanowire.

Edited by  
Weierstraß-Institut für Angewandte Analysis und Stochastik (WIAS)  
Leibniz-Institut im Forschungsverbund Berlin e. V.  
Mohrenstraße 39  
10117 Berlin  
Germany

Fax: +49 30 2044975  
E-Mail: [preprint@wias-berlin.de](mailto:preprint@wias-berlin.de)  
World Wide Web: <http://www.wias-berlin.de/>

## Abstract

We present a finite volume method for computing a representative range of eigenvalues and eigenvectors of the Schrödinger operator on a three dimensional cylindrically symmetric bounded domain with mixed boundary conditions. More specifically, we deal with a semiconductor nanowire which consists of a dominant host material and contains heterostructure features such as double-barriers or quantum dots. The three dimensional Schrödinger operator is reduced to a family of two dimensional Schrödinger operators distinguished by a centrifugal potential. Ultimately, we numerically treat them by means of a finite volume method. We consider a uniform, boundary conforming Delaunay mesh, which additionally conforms to the material interfaces. The  $1/r$  singularity is eliminated by approximating  $r$  at the vertexes of the Voronoi boxes. We study how the anisotropy of the effective mass tensor acts on the uniform approximation of the first  $K$  eigenvalues and eigenvectors and their sequential arrangement. There exists an optimal uniform Delaunay discretization with matching anisotropy. This anisotropic discretization yields best accuracy also in the presence of a mildly varying scattering potential, shown exemplarily for a nanowire resonant tunneling diode. For potentials with  $1/r$  singularity one retrieves the theoretically established first order convergence, while the second order convergence is recovered only on uniform grids with an anisotropy correction.

## 1 Introduction

As feature sizes of integrated circuits shrink to the nanometer scale, the device behavior changes since physical phenomena at short distances become dominant. In order to get good characteristics for scaled-down transistors, new transistor architectures have been developed progressively in the last decade. One of the promising architectures is the nanowire transistor [1, 2, 3, 4, 5, 6]. Semiconductor nanowires have also attracted much interest in opto-electronic applications [7, 8]. Based on nanowires, complex structures have been designed like nanowire resonant tunneling diodes [9, 10], multi-quantum-well nanowire heterostructures for lasers [11] as well as nanowire superlattices [12].

Basically a nanowire is a very thin cylinder of semiconductor materials. The functionality and performance of a nanowire device is determined by the design of the material heterostructure. Some modeling approaches are reviewed in Ref. [13]. Due to the feature length of the heterostructure which is in the order of magnitude of the mean free path of carriers, one uses the electronic Schrödinger equation for modeling the quantum phenomena. Moreover the effective mass approximation properly takes into account abrupt variations of the material properties on the nanometer scale. For some simple nanowire

heterostructures one can use an effective one dimensional model along the wire axis. More complex nanowire heterostructures still tend to be cylindrically symmetric and thus, require the solution of a family of Schrödinger equations in two dimensions which are distinguished by a centrifugal potential.

A challenge for modeling nanodevices is the open character of the quantum system, i.e. the active region of the nanowire is in contact with electrical leads. One can describe the charge transport between the leads by means of scattering theory. The scattering states are solutions of the electronic Schrödinger equation on unbounded real space. The direct computation of scattering states in two- and three-dimensional geometries requires a considerable computational effort [14, 15]. The R-matrix formalism [16, 17, 18, 19, 20, 21] is a potent means to reduce the computational costs. Indeed most of the computational effort of the R-matrix formalism stems from the Wigner–Eisenbud problem, that means an eigenproblem for the electronic Schrödinger operator in effective mass approximation on a bounded domain with mixed hard- and soft-wall boundary conditions. For complex heterostructures this eigenproblem has to be solved numerically and provides the Wigner–Eisenbud eigenfunctions and eigenenergies.

Our numerical approach to solve the Wigner–Eisenbud problem is based upon a 2D De-launay triangulation of the rotationally symmetric device domain and the finite volume method (FVM). Thus, we can describe any complex geometry and take the inhomogeneities and the anisotropy of the material properties into account. The combination of the FVM method for the Wigner–Eisenbud problem and the R-matrix formalism will allow the treatment of scattering problems in higher dimensions, as an alternative to the transparent boundary condition technique [22].

The structure of this paper is as following: In Sect. 2 we summarize shortly the finite volume method for cylindrical geometry and specify the approximations which apply here. In Sect. 3 we present the criteria for analyzing the accuracy of the numerical calculations for a representative range of eigenvalues and eigenvectors. In Sect. 4 we study a model problem without scattering potential, such that we can compare the numerical results with analytical ones. As it is suggested in Ref. [23], one has to study the influence of the finite element size and shape on the accuracy of the calculations. Moreover we investigate the influence of the anisotropy of the effective mass tensor. We generalize a result from Ref. [24, Sect. 5.3], where a second-order convergence of eigenvalues was observed in the case of an isotropic effective mass tensor and equilateral grids. We also numerically obtain second-order convergence of eigenvalues for an *anisotropic* effective mass tensor — at least for "mildly" varying potentials. For potentials with  $1/r$  singularity one retrieves the theoretically established first order convergence [24, Corollary 4.12], while the second order convergence is recovered only on uniform grids with an anisotropy correction. Sect. 5 deals exemplarily with a nanowire resonant tunneling diode. We demonstrate how a grid, optimized with respect to the geometry of the device and the material parameters, behaves in the presence of a double barrier potential.

One aim of this paper is to establish a procedure which provides ab initio an optimal uniform grid for the solution of the scattering problem within R-matrix formalism in complex nanowire geometries and material constellations. Thus, the extensive numerical

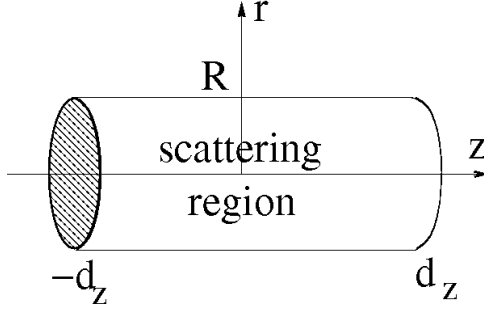


Figure 1: The scattering region of the cylindrically symmetric nanowire.

calculations can be performed on a fixed optimized grid. We are aware that an adaptive mesh refinement in the end provides better grids, but at higher computational costs and more programming effort.

## 2 Model

We consider nanowire devices, i.e. cylindrically symmetric semiconductor devices with a lead both at the top and the bottom of the cylinder. The semiconductor host material contains heterostructure features such as double-barriers or quantum dots. The distribution and the flow of charge carriers within these devices attract interest and can be derived from the electronic scattering states. In order to calculate these scattering states by means of the R-matrix method [20], one sets up the Wigner–Eisenbud problem which is an auxiliary eigenvalue problem on the scattering region, see Fig. 1.

### 2.1 Wigner–Eisenbud problem

The Wigner–Eisenbud problem comprises the calculation of the electronic states within the scattering region  $\tilde{\Omega}$  of the device closed up by hard- and soft-wall boundary conditions. For a heterostructure, one writes the stationary one-band electronic Schrödinger equation for the envelope function as

$$\left[ -\frac{\hbar^2}{2} \nabla \cdot (\mathbf{m}(\mathbf{r})^{-1} \nabla) + V(\mathbf{r}) \right] \Xi(\mathbf{r}) = E \Xi(\mathbf{r}), \quad (1)$$

where  $\mathbf{m}(\mathbf{r})$  is the position, i.e. material, dependent effective mass tensor. The potential energy  $V(\mathbf{r})$  generally includes the band-offsets of the heterostructure materials, the electron-electron interaction and the effect of an externally applied bias. The boundary conditions for Eq. (1) are homogeneous Neumann boundary conditions on the interfaces to the leads and homogeneous Dirichlet boundary conditions elsewhere. Let us consider a cylindrically symmetric system with the  $z$ -axis along the nanowire, such that  $\tilde{\Omega} = [0, R] \times [0, 2\pi] \times [-d_z, d_z]$ . For a semiconductor heterostructure with all crystal orientations such that the effective mass tensor is diagonal with respect to the cylindrical coordinates, one

has on  $\tilde{\Omega}$ :

$$\nabla \cdot (\mathbf{m}^{-1} \nabla) = \frac{1}{r} \frac{\partial}{\partial r} \left( \frac{r}{m_r^*(z, r)} \frac{\partial}{\partial r} \right) + \frac{1}{r^2} \frac{1}{m_r^*(z, r)} \frac{\partial^2}{\partial \theta^2} + \frac{\partial}{\partial z} \left( \frac{1}{m_z^*(z, r)} \frac{\partial}{\partial z} \right), \quad (2)$$

where  $m_r^*(z, r)$  and  $m_z^*(z, r)$  denote the position-dependent effective masses in the  $r$ - and  $z$ -direction, respectively. In case of a cylindrically symmetric potential, i.e.  $V(\mathbf{r}) = V(z, r)$ , the wave functions can be expressed in the form

$$\Xi(\mathbf{r}) = \frac{e^{im\theta}}{\sqrt{2\pi}} \chi(z, r), \quad m = 0, \pm 1, \pm 2, \dots, \quad (3)$$

where  $m$  is the magnetic quantum number and  $\chi(z, r)$  is the real-valued eigensolution of

$$\left\{ -\frac{\hbar^2}{2} \left[ \frac{1}{r} \frac{\partial}{\partial r} \left( \frac{r}{m_r^*(z, r)} \frac{\partial}{\partial r} \right) - \frac{1}{m_r^*(z, r)} \frac{m^2}{r^2} + \frac{\partial}{\partial z} \left( \frac{1}{m_z^*(z, r)} \frac{\partial}{\partial z} \right) \right] + V(z, r) \right\} \chi(z, r) = E \chi(z, r), \quad z, r \in \Omega = [-d_z, d_z] \times [0, R], \quad (4)$$

subject to the boundary conditions

$$\left. \frac{\partial \chi}{\partial z} \right|_{z=\pm d_z} = 0, \quad (5a)$$

$$\chi|_{r=R} = 0. \quad (5b)$$

The boundary condition at  $r = 0$ , arising from the reduction of the three-dimensional cylindrically symmetric problem to a two-dimensional problem, depends on the magnetic quantum number  $m$ ,

$$\left. \frac{\partial \chi}{\partial r} \right|_{r=0} = 0, \quad \text{for } m = 0, \quad (5c)$$

$$\chi|_{r=0} = 0, \quad \text{for } m \neq 0. \quad (5d)$$

Note the centrifugal potential  $\hbar^2 m^2 / (2m_r^* r^2)$  in Eq. (4). It arises from the angular kinetic energy and, by diverging at small  $r$ , forces the condition (5d) [25, Sect. 2.4].

The Wigner–Eisenbud problem is defined by the eigenvalue problem (4) with the boundary conditions (5).

Within a variational approach, the Wigner–Eisenbud problem is the condition under which the action integral

$$L = \int_{-d_z}^{d_z} \int_0^R r \left\{ \frac{\hbar^2}{2} \left[ \frac{1}{m_r^*} \left( \frac{\partial \chi}{\partial r} \right)^2 + \frac{1}{m_r^*} \frac{m^2}{r^2} \chi^2 + \frac{1}{m_z^*} \left( \frac{\partial \chi}{\partial z} \right)^2 \right] + (V - E) \chi^2 \right\} dr dz \quad (6)$$

has an extremum.

We now pass on to dimensionless variables. To that end, we introduce the scaling length  $l_0$  and the scaling energy  $u_0$

$$l_0 = 2d_z, \quad u_0 = \frac{\hbar^2}{2m_{z,\text{host}}^*} \left( \frac{\pi}{l_0} \right)^2, \quad (7)$$

where  $m_{z,\text{host}}^*$  is the effective mass in the  $z$ -direction of the host material. The effective masses are normalized to  $m_{z,\text{host}}^*$ . The dimensionless variables are denoted by a hat.

## 2.2 Discretization of the problem

There are different ways to discretize the Wigner–Eisenbud problem. For sufficiently regular geometries the approach in Ref. [20] is suitable, where the Wigner–Eisenbud eigenvalues and eigenfunctions were obtained by diagonalizing the matrix of the Wigner–Eisenbud Hamiltonian represented in an analytically obtained basis of functions. These basis functions are products of Bessel functions in  $r$ -direction (18) with cosine functions in  $z$ -direction (17). If the effective mass tensor depends nontrivially on the position, then the approach of Ref. [20] is not feasible anymore. That is why in this paper we consider a finite volume discretization based upon a boundary conforming Delaunay mesh of the scattering region which additionally conforms with the material interfaces. In our computational experiments we use uniform grids based on a tessellation of the domain  $\Omega$  by rectangles split by one of their diagonals. Thus, we regard a family of grids which is parameterized by the element size and its anisotropy. However, one can use just as well general Delaunay meshes as can be generated for instance by *Triangle* [26] or *TetGen* [27].

Based upon a Delaunay mesh we regard a finite volume discretization of problem (4) with the boundary conditions (5) which leads to a generalized eigenvalue problem of the form

$$\mathbf{H}\boldsymbol{\chi} = \mathbf{E}\mathbf{M}\boldsymbol{\chi}, \quad (8)$$

where  $\boldsymbol{\chi}$  is the vector with the nodal values of an eigenfunction,  $\mathbf{M}$  is the diagonal mass matrix of the Voronoi-box volumes with respect to the metric  $r dr dz$  and the stiffness

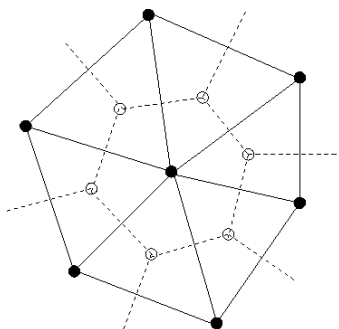


Figure 2: Sketch of the grid points (filled circles) and the Voronoi vertexes (empty circles) for a Delaunay triangulation.

matrix  $\mathbf{H}$  is the sum of the discretization  $\mathbf{S}$  of the kinetic part and the discretization  $\mathbf{U}$  of the potential energy part of the action integral (6). The matrix  $\mathbf{U}$  is the product of two diagonal matrices, namely the nodal values of the potential  $V$  and the mass matrix  $\mathbf{M}$ . For details see Appendix A. The global stiffness matrix  $\mathbf{H}$  is a real, sparse, symmetric, positive definite, band matrix. We are looking for eigenvectors of (8) which are normalized with respect to the scalar product

$$\langle \chi | \xi \rangle = \boldsymbol{\chi}^T \mathbf{M} \boldsymbol{\xi}, \quad (9)$$

where the superscript  $T$  denotes the transpose.

The variational formulation of the Schrödinger equation for rotationally symmetric geometries leads to a  $1/r$  singularity, see Eq. (6). One way to remove the singularity is to use the substitution  $\chi(r, z) = r\phi(r, z)$ , which leads to some complexity in the computation of finite-element matrices, but to the correct continuity of the solution [28, 29]. We use a different approach, namely we approximate the metric for the integrals over every element  $r dr dz \simeq r_V^{(e)} dr dz$  and  $1/r \simeq 1/r_V^{(e)}$ , where  $r_V^{(e)}$  is the  $r$ -coordinate of the circumcenter of the triangular element  $e$  and in turn are the vertexes of the Voronoi boxes, see Fig. 2. Thus, one can directly use the element matrices specific to Cartesian coordinates.

In the discretization (8) of the variational approach (6) only the Dirichlet boundary conditions (5b) and (5d) require special treatment. One can impose the homogeneous Dirichlet boundary conditions by means of a penalty method [30], i.e. by replacing the diagonal terms corresponding to the Dirichlet boundary nodes in the global stiffness matrix  $\mathbf{H}$  by a large number.

## 2.3 Convergence of eigensolutions

We are interested in the influence of the element shape and size on the accuracy of computed eigenvalues and eigenvectors of Eq. (4) with mixed boundary conditions (5). In Ref. [24], Corollary 4.12, the first order convergence of the eigenvalues of the Schrödinger operator with homogeneous Dirichlet boundary conditions on a domain  $\Omega \subset R^d$ ,  $d = 1, 2, 3$ , was proved

$$|E - E_{\text{ref}}| \leq Ch, \quad (10)$$

where  $h$  is the associated defining mesh size parameter and  $C$  is a mesh independent constant. For isotropically triangulated domains a computational analysis of model problems in Ref. [24] provided even second-order convergence

$$|E - E_{\text{ref}}| \leq Ch^2. \quad (11)$$

A second-order convergence of the eigenvalues for elliptic partial differential equations was also observed in Ref. [29] for finite element approximations of cylindrical geometries and the ansatz  $\chi(r, z) = r\phi(r, z)$ . Furthermore, for geometries where the symmetry axis is not included, e.g. coaxial waveguides, a quartic convergence is obtained for second-order polynomial finite element approximation.

In Ref. [24] the convergence of the eigenvectors is analyzed with respect to the  $L^2$ -norm. The R-matrix method requires to evaluate the eigenvectors for specific values of the spatial variables, more precisely at the interfaces to the leads. Therefore, we investigate the convergence of the eigenvectors with respect to the maximum norm. Furthermore, we analyze for cylindrical geometries the influence of the mesh anisotropy on the convergence rate.

We confirm for the problem at hand second order convergence (11) in the class of uniform grids with an anisotropy correction.

### 3 Setup of the computational experiments

For mesh generation we consider a uniform partition by a tensor mesh of the rectangular domain  $\hat{\Omega} = [-0.5, 0.5] \times [0, \hat{R}]$ , i.e. the basic elements are rectangles of the size  $h_z \times h_r$ . We define  $N_z = 1/h_z$  and  $N_r = \hat{R}/h_r$  such that the total number of the grid points is  $N = (N_z + 1) \times (N_r + 1)$ . We only regard partitions which conform with the material interfaces. Every rectangle is split into two triangles along the diagonal  $(0, h_r)(h_z, 0)$ . Thus, one obtains a uniform boundary conforming Delaunay triangulation. For this mesh, the mesh size parameter is given by

$$h = \sqrt{h_z^2 + h_r^2} \propto N^{-1/d}, \quad d = 2. \quad (12)$$

For the solution of the generalized eigenvalue problem (8), we use the iterative eigenvalue solver ARPACK [31] in the shift-invert mode with zero shift. It is most appropriate for large sparse matrices and is based upon the Implicitly Restarted Lanczos Method. For the shift-invert mode one needs a solver for a linear system of equations. Direct linear solvers like PARDISO [32, 33, 34] are advantageous for the sparse matrixes under consideration.

We now present the criteria by which we appraise our computational experiments. The first  $K$  eigensolutions of the generalized eigenvalue problem (8) are to be compared with either analytical reference solutions or validated numerical solutions of the original problem (4–5). We denote the reference eigenenergies with  $E_{l,\text{ref}}$  and the corresponding eigenvectors with  $\xi_l$  and investigate the relative errors of the eigenvalues

$$\varepsilon_l = \frac{E_l - E_{l,\text{ref}}}{E_{l,\text{ref}}}, \quad l = 1, \dots, K. \quad (13)$$

Sometimes we also regard the absolute error  $\Delta E_l = \varepsilon_l E_{l,\text{ref}}$  of the eigenvalue  $E_l$ .

In order to compare the numerical eigenvectors  $\chi_l$  with the reference eigenvectors  $\xi_l$  sampled at the nodal values, we introduce the relative error of the difference vector  $\chi_l - \xi_l$  with respect to the  $\ell^\infty$ -norm

$$\varepsilon_{l,\infty} = \frac{\|\chi_l - \xi_l\|_\infty}{\|\xi_l\|_\infty}, \quad l = 1, \dots, K. \quad (14)$$

The eigenvalues which are close to each other may be numerically interchanged. This can be verified by computing the scalar product between the reference eigenvector  $\xi_l$  and the

corresponding numerical eigenvector  $\chi_l$ . If their scalar product is close to zero,  $\langle \chi_l | \xi_l \rangle = 0$ , then the numerical eigenvalue  $E_l$  corresponds to another reference eigenvector  $\xi_{l'}$ , which yields a scalar product close to unity,  $\langle \chi_l | \xi_{l'} \rangle = \pm 1$ . The sum over the differences between the indexes of the corresponding numerical and reference eigenvectors

$$\delta = \sum_{l=1}^K |l - l'| \quad (15)$$

gives a global information about the accuracy of the numerical calculations, where  $l' = l$  if  $\langle \chi_l | \xi_l \rangle = \pm 1$ . The goal is to find a uniform convergence, i.e.  $|\Delta E_l| < |E_l - E_{l\pm 1}|$ . All the above holds for non-degenerate eigenvalues. In case of degeneracy special care has to be taken.

## 4 Wigner–Eisenbud problem without scattering potential

We consider a nanowire with radius  $R = 5$  nm, length  $2d_z = 32$  nm and with a mass tensor that does not depend on the space variables, i.e.  $m_z^*(z, r) = m_z^* = m_{z, \text{host}}^*$  and  $m_r^*(z, r) = m_r^*$ . Furthermore, the particles are neither confined by any additional potential in the domain nor do they interact with each other, i.e.  $V(z, r) \equiv 0$ . For the effective masses we consider five cases: i)  $m_z^* = m_r^* = 0.067m_0$ , as for GaAs; ii)  $m_z^* = 0.19m_0$ ,  $m_r^* = 0.98m_0$ , and iii)  $m_z^* = 0.98m_0$ ,  $m_r^* = 0.19m_0$  as for Si; iv)  $m_z^* = 0.08m_0$ ,  $m_r^* = 1.6m_0$ , and v)  $m_z^* = 1.6m_0$ ,  $m_r^* = 0.08m_0$  as for Ge, where  $m_0$  is the free electron mass. We study the first  $K = 150$  eigensolutions.

The analytical solutions of Eq. (4) with  $V(z, r) \equiv 0$  and mixed boundary conditions (5) can be found by the separation of variables method,

$$\xi_l(z, r) = u_i(z)v_j(r), \quad E_l = E_{i,z} + E_{j,r}, \quad l = 1, 2, 3, \dots \quad (16)$$

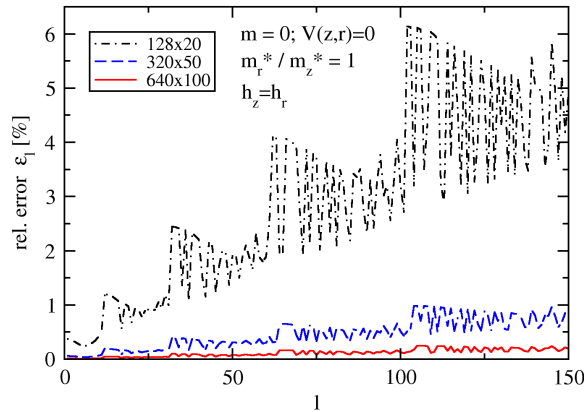


Figure 3: Relative errors for the lowest 150 eigenvalues in the isotropic case for different equilateral grids specified in the legend as  $N_z \times N_r$ .

The eigenvalues and eigenfunctions of the longitudinal eigenvalue problem are

$$E_{i,z} = \frac{\hbar^2}{2m_z^*} \left( \frac{i\pi}{2d_z} \right)^2 = i^2 u_0, \quad u_i(z) = \frac{1}{\sqrt{2d_z}} \begin{cases} 1, & i = 0, \\ \sqrt{2} \cos \left( \frac{i\pi(z+d_z)}{2d_z} \right), & i = 1, 2, 3, \dots \end{cases} \quad (17)$$

where  $u_0$  is the scaling energy (7). The eigenvalues and eigenfunctions of the radial eigenvalue problem are

$$E_{j,r} = \frac{\hbar^2}{2m_r^*} \left( \frac{x_{mj}}{R} \right)^2 = \frac{m_z^*}{m_r^*} \left( \frac{x_{mj}}{\hat{R}} \right)^2 \frac{u_0}{\pi^2}, \quad v_j(r) = \frac{\sqrt{2}}{R J_{|m|+1}(x_{mj})} J_m \left( x_{mj} \frac{r}{R} \right), \quad j = 1, 2, 3, \dots, \quad (18)$$

where  $J_m$  is the Bessel function of first kind,  $x_{mj}$  is the  $j$ th root of  $J_m(x)$  and  $\hat{R} = R/l_0$ .

## 4.1 Analysis of the eigenvalues

In Fig. 3 we present the relative errors  $\varepsilon_l$ , see Eq. (13), in the isotropic case  $m_z^* = m_r^*$  with the magnetic quantum number  $m = 0$  for different equilateral (i.e.  $h_z = h_r$ ) grids. Unsurprisingly, by refining the grid, the number of the lowest eigenvalues that are satisfactorily computed increases, because the dimension of the generalized eigenvalue problem increases, so that the matrix elements approximate better the action integral.

We present in Fig. 4 the influence of the ratio  $m_r^*/m_z^*$  between the effective masses on the relative errors  $\varepsilon_l$  in the case of a fixed equilateral grid. We plotted the envelopes as shaded areas between the minimum and the maximum values. The relative error increases with the order  $l$  of the eigenvalue and with the anisotropy of the effective mass tensor.

Another observation is that the upper envelopes for the case  $m_r^*/m_z^* > 1$  exhibit several jumps. These jumps are due to changes of the eigenenergies from  $E_l = E_{i,z} + E_{j,r}$  to  $E_{l+1} = E_{0,z} + E_{j+1,r}$ , i.e. another ladder of  $E_{i,z}$  values starts superimposed on the next  $E_{j+1,r}$  value. In the case  $m_r^*/m_z^* < 1$  the lower envelope behaves correspondingly. Hence, for the studied system, by watching the run of the upper and lower envelopes of the curves, one can see which of the absolute errors  $\Delta E_z$  and  $\Delta E_r$  contributes to the absolute error  $\Delta E$  to a greater extent.

Fig. 5 shows the relative errors for the lowest ten eigenvalues versus the total number of grid points  $N$ . If the magnetic quantum number  $m$  is zero, we numerically obtain a second-order convergence,  $\varepsilon_l \propto h^2 \propto N^{-2/d}$ , note  $d = 2$ , for the eigenvalues of the Wigner–Eisenbud problem for cylindrically symmetric systems. This result applies to the class of equilateral grids and is independent on the ratio  $m_r^*/m_z^*$ . Considering a centrifugal potential, i.e.  $m \neq 0$ , the convergence rate deviates from the second-order and gets closer to the first order.

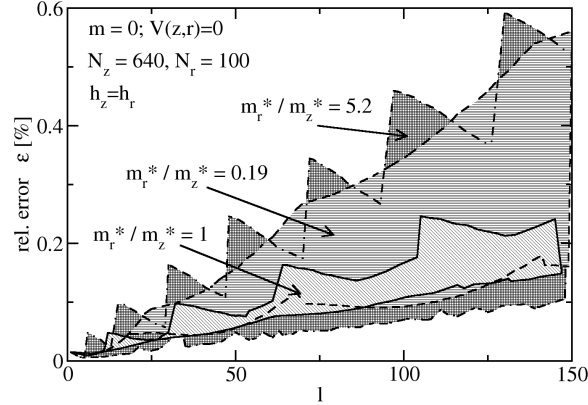


Figure 4: Relative errors for the lowest 150 eigenvalues for different ratios  $m_r^*/m_z^*$  computed on an equilateral grid with  $N_z = 640$  and  $N_r = 100$ .

## 4.2 Analysis of the eigenvectors

We present in Fig. 6 the scalar product  $\langle \chi_l | \xi_l \rangle$  between the normalized numerical eigenvectors  $\chi_l$  and the analytical eigenvectors  $\xi_l$ , see Eq. (9), for a fixed equilateral grid and for magnetic quantum numbers  $m = 0$  and  $|m| = 1$ . The scalar products  $\langle \chi_l | \xi_l \rangle$  are very close to unity. Deviations from unity give a measure for the accuracy of the numerical eigenvectors. Refining the grid, for equilateral or non-equilateral grids, the scalar products get closer to unity.

We present in Fig. 7 the relative errors  $\varepsilon_{l,\infty}$ , Eq. (14). Refining the grid, these errors get smaller for the whole range of the eigenvectors. As expected, there are eigenvectors which are computed more accurately than others for a specific grid, yielding the minima in  $\varepsilon_{l,\infty}$ .

We present in Fig. 8 the total number of order-interchanges  $\delta$ , Eq. (15), versus the number of grid points  $N$ . Increasing the number of grid points, the number of order-interchanges decreases. For an equilateral grid, there are least order-interchanges if the effective mass tensor is isotropic.

## 4.3 Influence of the element size and shape

We study further the effect of refining the grid in  $r$ -direction, while keeping a fixed discretization in  $z$ -direction. We plot in Fig. 9(a) the absolute errors for the lowest ten eigenvalues for this refining method. For higher eigenvalues, there is a saturation of the error in dependence of the grid refining. This can be understood by considering that we study a separable case, see (16), so that the absolute error can be separated also in the absolute errors for computing the eigenvalues in each direction. For a uniform grid, one has for every direction a second-order convergence like in the one dimensional case [24]

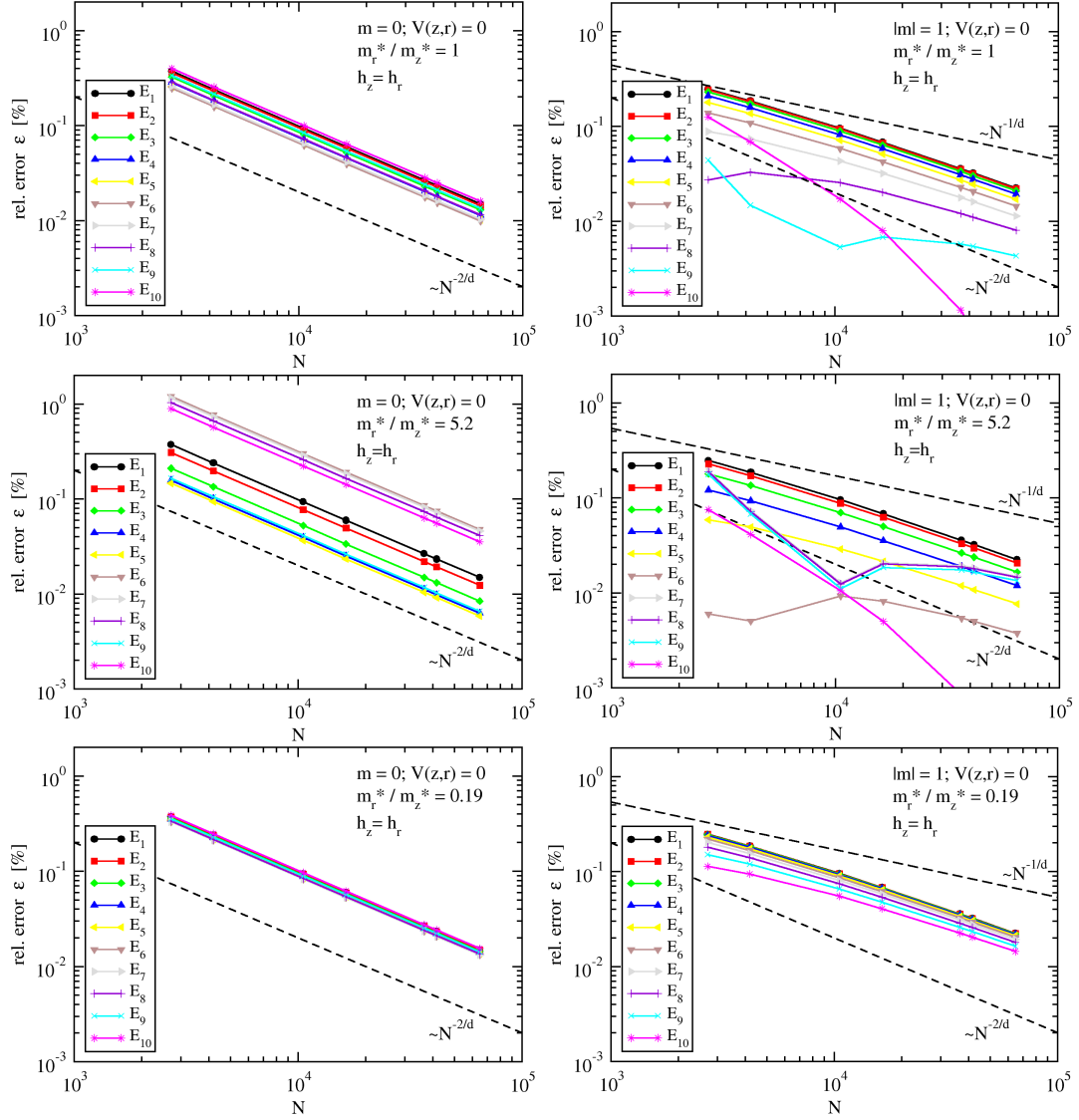


Figure 5: Relative errors for the lowest ten eigenvalues vs. the number of grid points  $N$ , for magnetic quantum numbers  $m = 0$  (left) and  $|m| = 1$  (right), for equilateral grids and different ratios  $m_r^*/m_z^*$  of the effective masses.

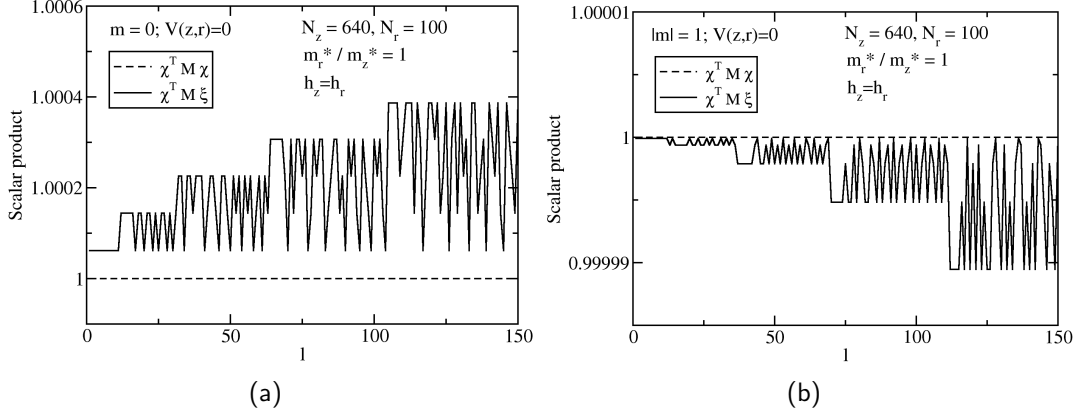


Figure 6: Scalar product (9) between the analytical  $\xi_l$  and numerical  $\chi_l$  eigenvectors for a fixed equilateral grid and for (a)  $m = 0$  and (b)  $|m| = 1$ .

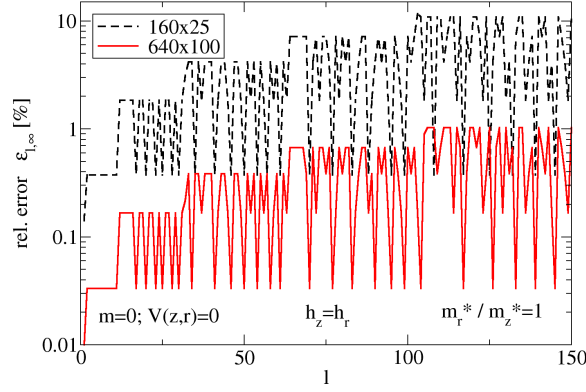


Figure 7: Relative errors for  $l^\infty$ -norm (14) of the difference between the analytical and the numerical eigenvectors  $\chi_l - \xi_l$ , for a coarse and a fine equilateral grid and for  $m = 0$ .

such that

$$\Delta E_l = \varepsilon_l E_l = \Delta E_{i,z} + \Delta E_{j,r} \propto C_{i,z} h_z^2 + C_{j,r} h_r^2 \propto \frac{1}{N_z^2} + \alpha_l \frac{\hat{R}^2}{N_r^2}. \quad (19)$$

The prefactor  $\alpha_l$  depends on the order  $l$ , which is a specific combination between the orders  $(i, j)$  in  $z$  and  $r$ -direction, respectively. The above dependence versus the total number of grid points  $N$  is plotted in Fig. 9(b) and explains qualitatively the behavior in Fig. 9(a). The error saturates when the mesh distance in one direction is much smaller than in the other direction, because the coarser grid establishes the total error of the eigenvalue  $E_l$ .

Further we consider different grids with the same number  $N_{\text{el}} = 2N_z N_r = 128000$  of finite elements implying almost the same number  $N = (N_z + 1) \times (N_r + 1)$  of grid points. This is equivalent to considering grids with the same element sizes, i. e. the same element area  $A = h_z h_r / 2 = R / N_{\text{el}}$ , but with different aspect ratio,  $h_z / h_r$ . Thus, one

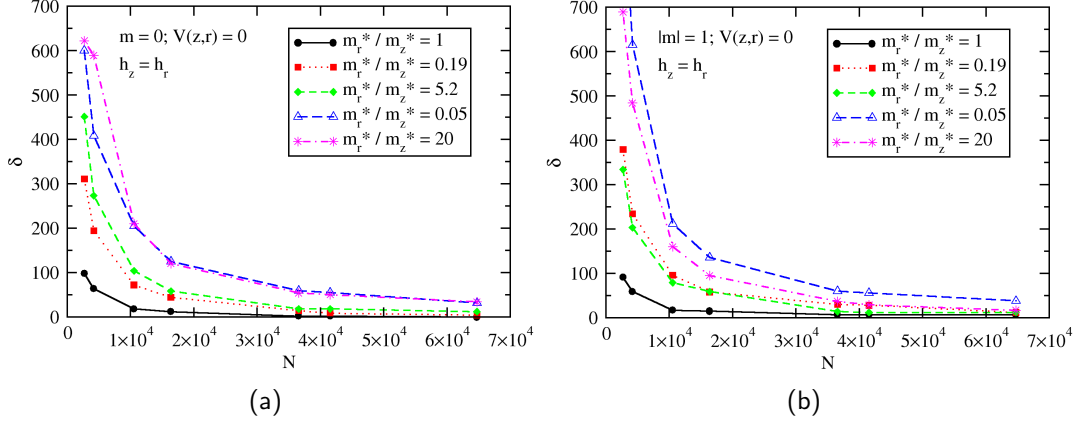


Figure 8: Total number of order-interchanges (15) depending on grid fineness (measured by  $N$ ), for different anisotropy of the effective mass tensor and for (a)  $m = 0$  and (b)  $|m| = 1$ .

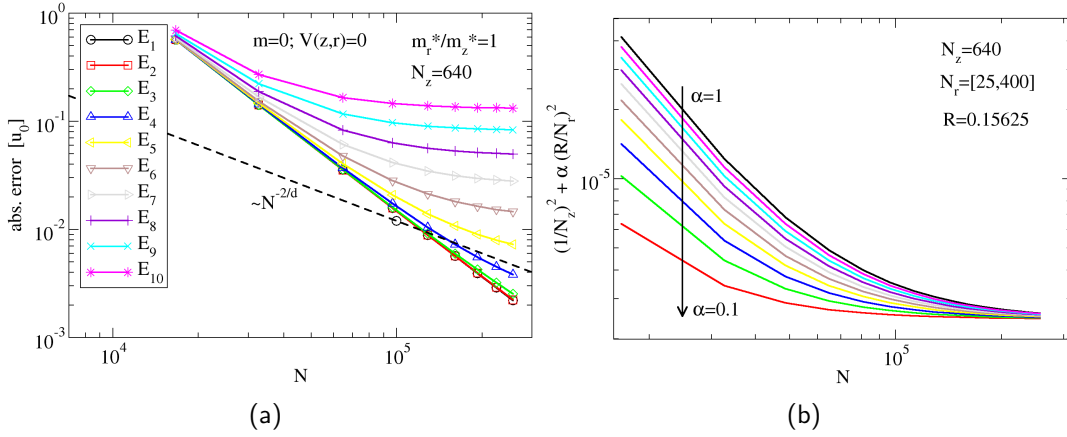


Figure 9: (a) Absolute errors for the lowest ten eigenvalues, and (b) the absolute error for a separable problem (see Eq. (19)) versus  $N$  for a fixed  $N_z = 640$  and refining  $N_r$ ,  $N_r = 25, 50, 100, 150, 200, 250, 300, 350$  and  $400$ .  $\alpha$  varies in steps of  $0.1$ .

has

$$\frac{h_z}{h_r} \propto h_z^2 \quad \text{and} \quad \frac{h_z}{h_r} \propto \frac{1}{h_r^2}. \quad (20)$$

We present in Fig. 10 the relative errors  $\varepsilon_l$  versus the aspect ratio  $h_z/h_r$ , for the eigenvalues obtained as combinations between the lowest eigenvalue in the  $r$ -direction, i.e.  $E_{1,r}$ , and the lowest ten eigenvalues in the  $z$ -direction, i.e.  $E_{i,z}$  with  $i = 1, \dots, 10$  and for different anisotropy of the effective mass tensor.

The problem at hand is separable so that the absolute error can also be separated,  $\Delta E_l = \Delta E_{i,z} + \Delta E_{j,r}$ . For  $h_z/h_r \ll 1$ , i.e. larger mesh grid in  $r$ -direction, the error  $\Delta E_{j,r}$ , which is quadratic in  $h_r$ , dominates the error  $\Delta E_l$ . One can clearly see the linear decrease of  $\Delta E_l$  with  $h_z/h_r \propto 1/h_r^2$  in Fig. 10. On the other hand for  $h_z/h_r \gg 1$ , the linear increase of  $\Delta E_l$  with  $h_z/h_r \propto h_z^2$  reflects the dominance of  $\Delta E_{i,z}$  (at least

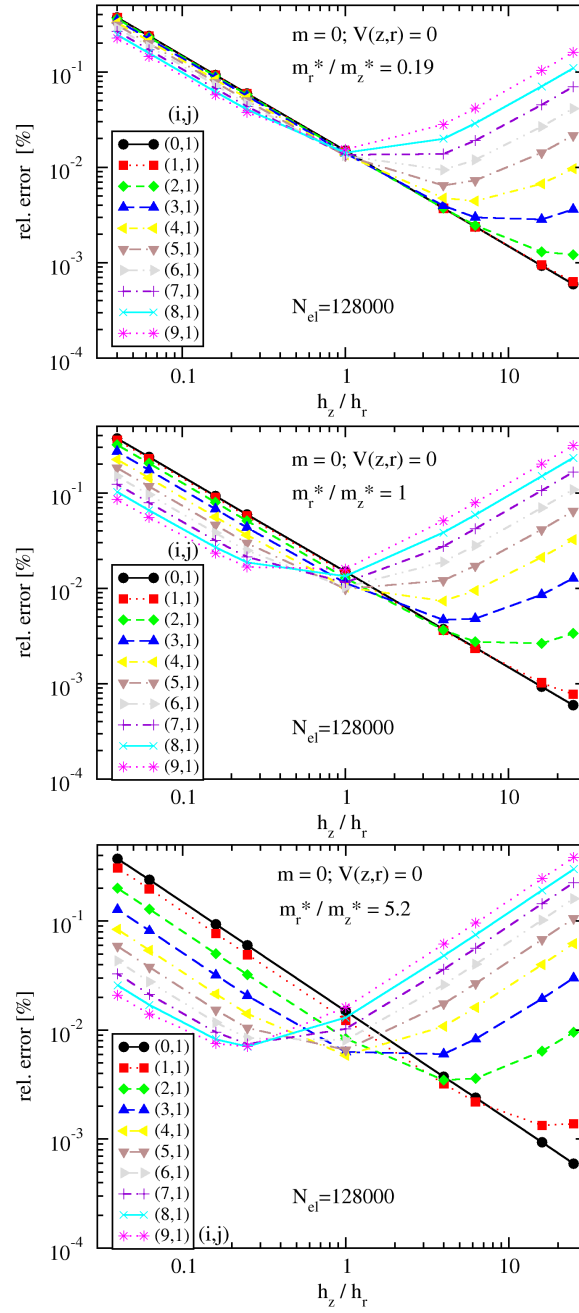


Figure 10: The relative errors for the eigenvalues obtained as combinations of the lowest eigenvalue in the  $r$ -direction and lowest ten eigenvalues in the  $z$ -direction vs. the ratio of the mesh sizes keeping the area of the finite elements constant, for different anisotropy of the effective mass tensor.

if  $i$  is high enough) which is quadratic in  $h_z$ , see (11). Although only the case  $j = 1$  is shown here, the behavior for other  $j$  values is the same. The linear decrease of  $\Delta E_1 = \Delta E_{1,r} + \Delta E_{0,z}$  with  $h_z/h_r \propto 1/h_r^2$  is due to  $E_{0,z} = 0$ .

In Fig. 11 we present the total number of order-interchanges versus the aspect ratio  $h_z/h_r$  for different anisotropy of the effective mass tensor. In any case, there exists an optimal aspect ratio  $h_z/h_r$  for which the number of order interchanges is minimal. If  $K$  takes large values, the minimum value of the order-interchanges increases, but qualitatively the dependence of  $\delta$  on  $h_z/h_r$  remains the same. The position of the minimum depends on the ratio between the effective masses  $m_z^*/m_r^*$ .

Since the eigenvalue problem is separable, the eigenvalues are sums of the eigenvalues corresponding to the directions  $z$  and  $r$ , see Eq. (16).

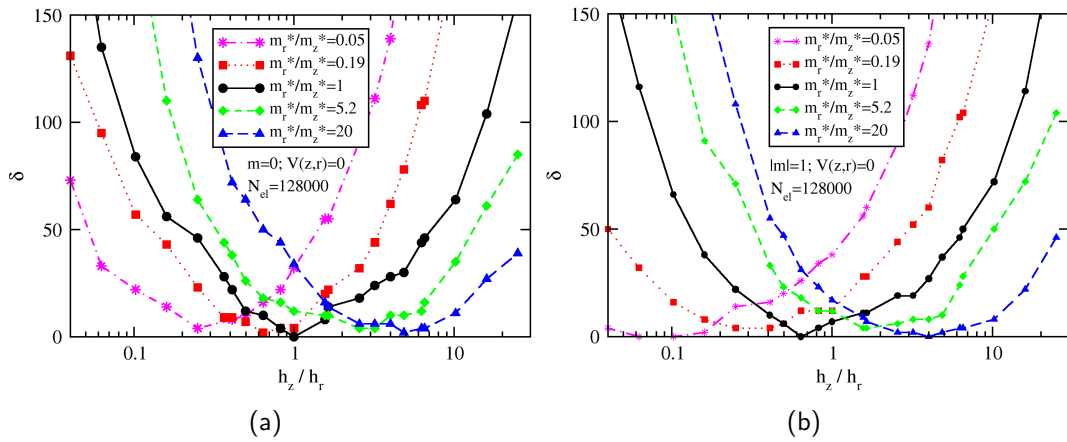


Figure 11: Total number of order-interchanges as function of the aspect ratio  $h_z/h_r$  keeping the area of the finite elements constant with regard to different anisotropy of the effective mass tensor. These dependences are shown for different magnetic quantum numbers (a)  $m = 0$  and (b)  $|m| = 1$ .

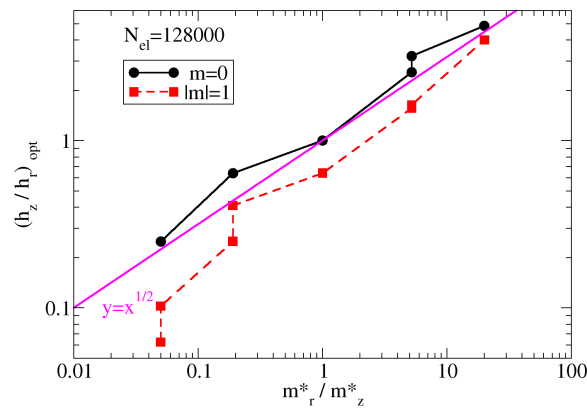


Figure 12: Dependence of the optimal aspect ratio  $h_z/h_r$  of the grid on the effective masses ratio  $m_r^*/m_z^*$ , for different magnetic quantum numbers  $m$ .

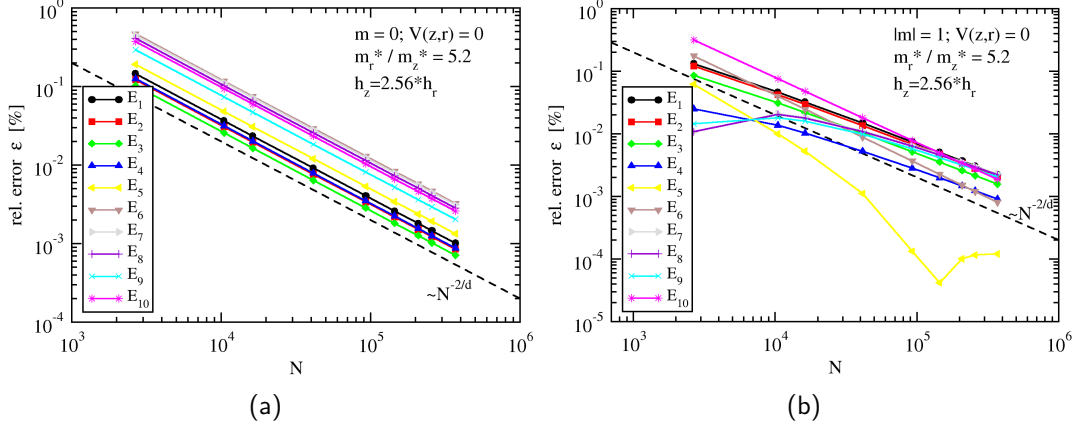


Figure 13: Relative errors for the lowest ten eigenvalues considering a grid with the optimal aspect ratio  $h_z/h_r = 2.56 \simeq 2.28 = (m_r^*/m_z^*)^{1/2}$  for (a)  $m = 0$  and (b)  $|m| = 1$ . One catches the optimal value only approximately, due to the discreteness of the problem.

The eigenvalues in the  $r$ -direction,  $E_{j,r}$ , depend inversely proportional on the ratio  $m_r^*/m_z^*$ , see Eq. (18). For  $m_r^*/m_z^* > 1$  these values decrease and clot. In order to avoid order-interchanges, the  $r$ -direction must be better resolved, i. e.  $h_r < h_z$ . Fig. 12 reveals that in the case of the Schrödinger equation in cylindrical coordinates without scattering potential the optimal aspect ratio is given by  $(h_z/h_r)_{\text{opt}} = (m_r^*/m_z^*)^{1/2}$ . This relation is obtained asking for equal errors for the eigenvalues in each direction, see Eqs. (17) and (18):  $\Delta i^2 = \Delta x_{m_j}^2$ , or  $h_z^2 m_z^* = h_r^2 m_r^*$ .

One recovers the second-order convergence of the eigenvalues while refining the grid in such a way that the anisotropy of the grid and of the effective mass tensor match perfectly, as shown in Fig. 13. Up to now we have investigated the Wigner–Eisenbud problem without a scattering potential yet for the scale of magnetic quantum numbers  $m = \pm 1$ , such that a centrifugal potential is taken into account. Now we are going to study the influence of a perturbation by an external potential using the example of a nanowire resonant tunneling diode.

## 5 Wigner–Eisenbud problem for a nanowire resonant tunneling diode

In this section we study the first  $K = 150$  eigenvalues and eigenvectors of problem (4) - (5) for a nanowire resonant tunneling diode. More precisely, we consider a double barrier potential along a nanowire (DBNW) as described in Sect. 4, see Fig. 14. The height of the barriers is  $V_0 = 0.5$  eV and the width  $b = 4$  nm. The width of the quantum well is  $w = 8$  nm. To begin with, we consider equal and position independent effective masses,  $m_r^* = m_z^* = 0.19m_0$ .

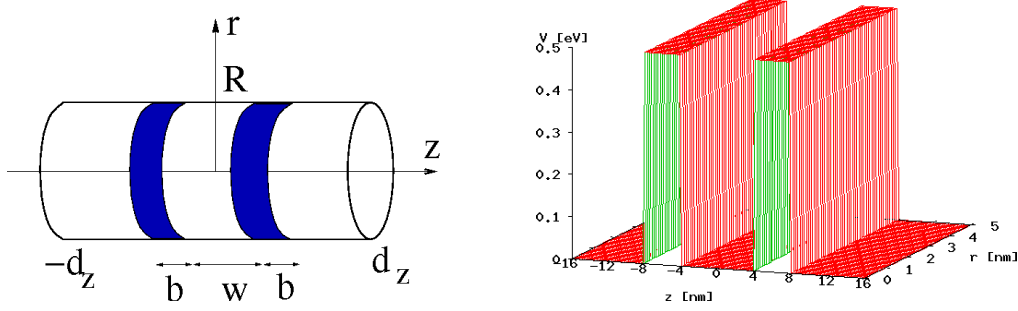


Figure 14: Sketch of a double barrier nanowire (DBNW) together with the scattering potential  $V(z, r)$ . For instance, such a structure is used as a resonant tunneling diode.

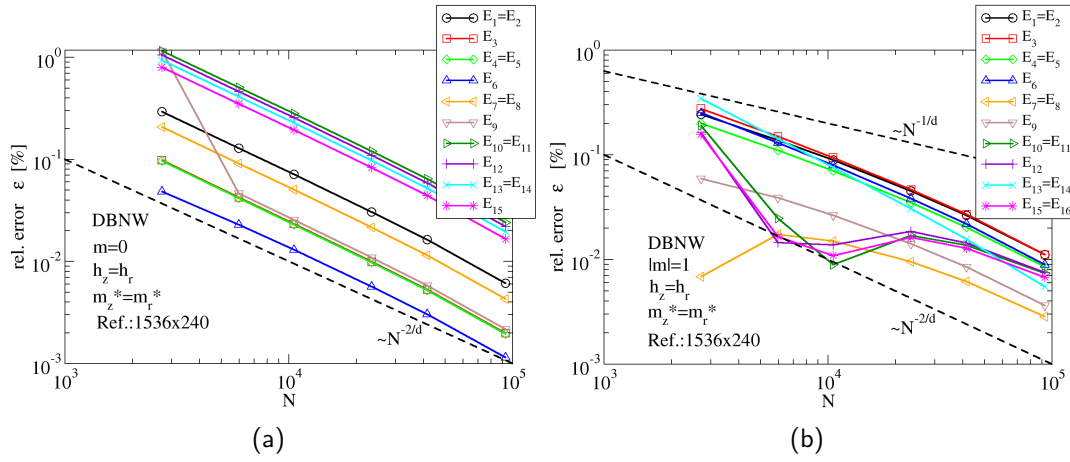


Figure 15: Relative errors for the lowest ten eigenvalues for the nanowire resonant tunneling diode versus total number of grid points  $N$ , for (a)  $m = 0$  and (b)  $|m| = 1$ .

We consider a validated reference solution obtained by means of the method proposed in this paper with a sufficiently large number of grid points, at least  $N_z \times N_r = 1536 \times 240$ . The accuracy of the eigenvalues and eigenvectors is similar to the case of Sect. 4. Second-order convergence of the eigenvalues is recovered for the case of a nanowire resonant tunneling diode for magnetic quantum number  $m = 0$ , see Fig. 15. If  $m \neq 0$  we have at least the theoretically predicted first order convergence. Some of the Wigner–Eisenbud energies are degenerated, i.e.  $E_1 = E_2$ , because the structure is symmetric with respect to  $z = 0$ .

The scalar product between the numerical and the reference eigenvectors is very close to unity for the whole range of the studied eigenvectors. This allows us to order the eigenvectors and in Fig. 16 we plot the total number of order-interchanges for different equilateral grids. Refining the grid, in this case uniformly, the number of interchanges reaches zero indicating very accurate numerical calculations.

In order to study the influence of the aspect ratio  $h_z/h_r$  of the grid on the accuracy of the numerical calculations, we plot in Fig. 17 the total number of order-interchanges versus  $h_z/h_r$ . The grids are generated such that the total number of elements remains fixed,

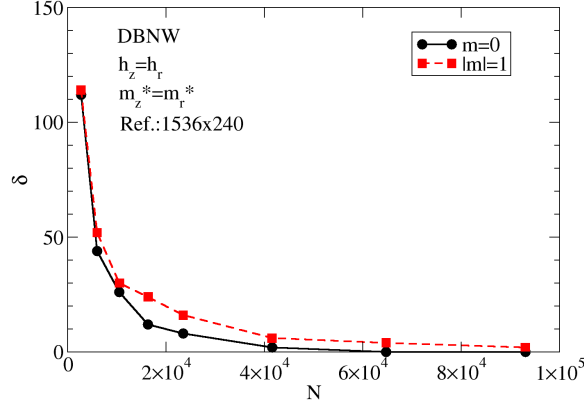


Figure 16: Total number of order-interchanges (15) versus number of grid points  $N$  for the nanowire resonant tunneling diode.

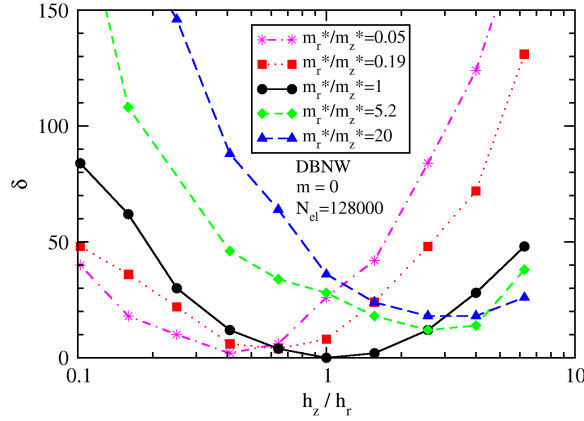


Figure 17: Total number of order-interchanges (15) for a nanowire resonant tunneling diode versus the aspect ratio of the grids with  $N_{\text{el}} = 128000$  and for  $m = 0$ . Different anisotropies of the effective mass tensor are considered.

$N_{\text{el}} = 128000$ . We also consider, as in the previous section, an anisotropic host material, but we keep the effective masses in the barriers constant, i.e.  $m_{r,b}^* = m_{z,b}^* = 0.19m_0$ . Again, the optimal aspect ratio of the discretization depends on the anisotropy of the effective mass tensor. The optimal aspect ratio is  $(h_z/h_r)_{\text{opt}} = (m_r^*/m_z^*)^{1/2}$ . This is the same result as in the case without scattering potential, see Fig. 18.

Notwithstanding the influence of the heterostructure potential the fundamental properties of the discretization of the Wigner–Eisenbud Hamiltonian for systems with cylindrical symmetry still apply.

## 6 Conclusions

We have presented a finite volume discretization of a cylindrically symmetric Wigner–Eisenbud problem, for computing a representative part of the spectral decomposition

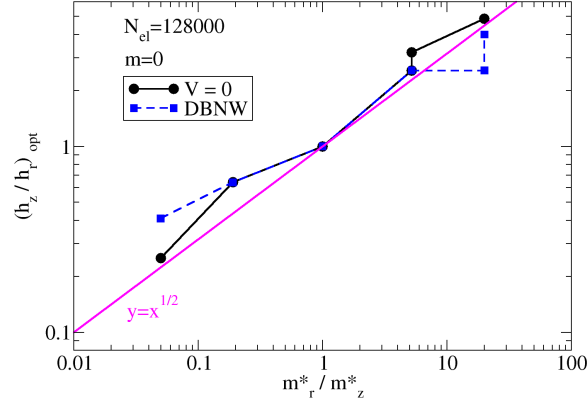


Figure 18: The optimal aspect ratio  $(h_z/h_r)_{\text{opt}}$  for the Wigner–Eisenbud problem for a cylindrical nanowire first without scattering potential ( $V = 0$ ) and second with a double barrier potential (DBNW).

of a two-dimensional radial Schrödinger operator with mixed boundary conditions on a bounded domain. We have used linear triangular finite elements, uniformly structured meshing and the lumping approximation for the scattering and centrifugal potential in the variational formulation of the problem. In order to remove the  $1/r$  singularity for rotationally symmetric geometries we have approximated over every element  $r$  with the  $r$ -coordinate of the circumcenter of the triangular element  $e$ .

Criteria for determining the accuracy of the numerical method for a prescribed range of eigenvalues and eigenvectors have been established. We have introduced the total number of order-interchanges as a global quantity that describes the accuracy of the approximation. Based on the geometry of the structure and on the effective mass tensor of the host material one can set up an optimal grid, a grid which serves equally satisfactorily all the calculations with a variety of scattering potentials. These include the Coulomb potential and the exchange-correlation potential. One has to be more careful with an additional confinement potential as in quantum dots. However, this potential can be feeded into the initial set-up.

The optimal shape (i.e. aspect ratio) of the triangular elements is determined by the anisotropy of the effective mass tensor, namely  $(h_z/h_r)_{\text{opt}} = (m_r^*/m_z^*)^{1/2}$ , while the mesh size can be chosen according to the second-order convergence of the eigenvalues in tune with the required accuracy. Thus, for *cylindrically symmetric systems* we generalize a result from Ref. [24], where a second-order convergence of the eigenvalues was observed in the case of an isotropic effective mass tensor and equilateral grids.

This study presents a versatile and effective numerical method for the solution of the Wigner–Eisenbud problem for complex semiconductor nanowire devices. This paves the way for solving the three-dimensional scattering problem for such devices. Thus, we provide a tool for the electronic modeling of real-world semiconductor nanostructures.

## 7 Acknowledgments

We thank our colleagues Klaus Gärtner, Thomas Koprucki and Rüdiger Müller for useful discussions.

## A Linear triangular elements

The finite element method seeks an approximation  $\chi^{(e)}(z, r)$  to the exact solution  $\chi(z, r)$  in each of the elements. We consider triangular finite elements with the dimensionless coordinates of the nodes in the counter-clockwise order,  $(\hat{z}_1, \hat{r}_1)$ ,  $(\hat{z}_2, \hat{r}_2)$  and  $(\hat{z}_3, \hat{r}_3)$ . The most common form for a representation of the element approximation  $\chi^{(e)}$  is the linear approximation. Following the standard finite element method approximation for linear triangular elements [35, 36] one obtains the contribution of one element to the action integral (6)

$$L_e = \boldsymbol{\chi}_e^T \mathbf{S}_e \boldsymbol{\chi}_e + \boldsymbol{\chi}_e^T \mathbf{U}_e \boldsymbol{\chi}_e - E \boldsymbol{\chi}_e^T \mathbf{M}_e \boldsymbol{\chi}_e,$$

where  $\boldsymbol{\chi}_e^T = (\chi_1 \ \chi_2 \ \chi_3)$  are the vectors with the nodal values,  $\mathbf{S}_e$  is the kinetic part of the stiffness matrix of the finite element,  $\mathbf{U}_e$  is the scattering potential energy part of the stiffness matrix, and  $\mathbf{M}_e$  is the mass matrix of the finite element. By means of the *lumping* approximation the matrixes  $\mathbf{U}_e$  and  $\mathbf{M}_e$  become diagonal, see Sect. 2.2. We have  $\mathbf{U}_e = f \mathbf{S}_V$  and  $\mathbf{M}_e = f \mathbf{S}_E$ , with  $f = J \hat{r}_U^{(e)}$  where

$$J = (\hat{z}_2 - \hat{z}_1)(\hat{r}_3 - \hat{r}_1) - (\hat{z}_3 - \hat{z}_1)(\hat{r}_2 - \hat{r}_1)$$

is the Jacobian of the linear transformation of the triangular element into the right unit triangle in the natural coordinate system  $(\xi, \eta)$  [35, Sect. 2.2.1]. The  $r$ -coordinate of the circumcenter of a triangular element is

$$\hat{r}_U^{(e)} = [(\hat{z}_1^2 + \hat{r}_1^2)(\hat{z}_3 - \hat{z}_2) + (\hat{z}_2^2 + \hat{r}_2^2)(\hat{z}_1 - \hat{z}_3) + (\hat{z}_3^2 + \hat{r}_3^2)(\hat{z}_2 - \hat{z}_1)] / D$$

with  $D = 2[\hat{z}_1(\hat{r}_2 - \hat{r}_3) + \hat{z}_2(\hat{r}_3 - \hat{r}_1) + \hat{z}_3(\hat{r}_1 - \hat{r}_2)]$ . Furthermore we have

$$\mathbf{S}_V = \begin{pmatrix} A_1 V_1 & 0 & 0 \\ 0 & A_2 V_2 & 0 \\ 0 & 0 & A_3 V_3 \end{pmatrix}, \quad \mathbf{S}_E = \begin{pmatrix} A_1 & 0 & 0 \\ 0 & A_2 & 0 \\ 0 & 0 & A_3 \end{pmatrix},$$

where  $A_i$ ,  $i = 1, 2, 3$  are the areas in the  $(\xi, \eta)$ -coordinates of the subdomains obtained connecting the circumcenter with the midpoints of the edges. One has

$$A_1 = \frac{1}{4} \xi_u + \frac{1}{4} \eta_u, \quad A_2 = \frac{1}{4} - \frac{1}{4} \xi_u, \quad A_3 = \frac{1}{4} - \frac{1}{4} \eta_u,$$

where  $(\xi_u, \eta_u)$  are the transformed coordinates of the circumcenter. The values  $V_i$ ,  $i = 1, 2, 3$  are the potential nodal values. For the matrix  $\mathbf{S}_e$  we use the same expression as for Cartesian coordinates given in [36, Sect. 5.2 and 7.2]

$$\mathbf{S}_e = \frac{D_z}{2J} \begin{pmatrix} b_1^2 & b_1 b_2 & b_1 b_3 \\ b_2 b_1 & b_2^2 & b_2 b_3 \\ b_3 b_1 & b_3 b_2 & b_3^2 \end{pmatrix} + \frac{D_r}{2J} \begin{pmatrix} c_1^2 & c_1 c_2 & c_1 c_3 \\ c_2 c_1 & c_2^2 & c_2 c_3 \\ c_3 c_1 & c_3 c_2 & c_3^2 \end{pmatrix} + \frac{JG}{24} \begin{pmatrix} 2 & 1 & 1 \\ 1 & 2 & 1 \\ 1 & 1 & 2 \end{pmatrix},$$

with  $b_i = \hat{r}_j - \hat{r}_k$ , and  $c_i = \hat{z}_k - \hat{z}_j$ , where the triple  $(i, j, k)$  is a cyclic permutation of  $(1, 2, 3)$  and

$$D_z = \frac{1}{\pi^2} \frac{1}{\hat{m}_z^{*(e)}} \hat{r}_U^{(e)}, \quad D_r = \frac{1}{\pi^2} \frac{1}{\hat{m}_r^{*(e)}} \hat{r}_U^{(e)}, \quad G = \frac{1}{\pi^2} \frac{m^2}{\hat{m}_r^{*(e)}} \frac{1}{\hat{r}_U^{(e)}}.$$

The effective masses  $\hat{m}_z^{*(e)}$  and  $\hat{m}_r^{*(e)}$  are constant over a finite element. The last term in  $\mathcal{S}_e$  comes from the centrifugal potential. In order to be consistent with the lumping approximation, it is approximated by the form  $JG\mathcal{S}_E$ .

We use the so-called *direct stiffness matrix method* [36] in order to incorporate the element stiffness matrices into the global stiffness matrix

$$\mathbf{H} = \sum_{e=1}^{N_{\text{el}}} (\mathbf{S}_e + \mathbf{U}_e),$$

where  $N_{\text{el}}$  is the number of the finite elements.

The finite element method in two dimensions with the lumping approximation is equivalent to the finite volume method.

## References

- [1] Y. Cui, Z. Zhong, D. Wang, W. U. Wang, and C. M. Lieber. High performance silicon nanowire field effect transistors. *Nano Lett.*, 3:149, 2003.
- [2] Jie Xiang, Wei Lu, Yongjie Hu, Yue Hu, Hao Yan, and Charles M. Lieber. Ge/Si nanowire heterostructures as high-performance field-effect transistors. *Nature*, 441:489, 2006.
- [3] Tomas Bryllert, Lars-Erik Wernersson, Truls Loewgren, and Lars Samuelson. Vertical wrap-gated nanowire transistors. *Nanotechnology*, 17:S227, 2006.
- [4] G. Liang, J. Xiang, N. Karche, G. Klimeck, C. M. Lieber, and M. Lundstrom. Performance analysis of a Ge/Si core/shell nanowire field effect transistor. *Nano Lett.*, 7:642, 2007.
- [5] K. H. Cho, Y. C. Jung, B. H. Hong, S. W. Hwang, J. H. Oh, D. Ahn, S. D. Suk, K. H. Yeo, D.-W. Kim, D. Park, and W.-S. Lee. Observation of three-dimensional shell filling in cylindrical silicon nanowire single electron transistors. *Appl. Phys. Lett.*, 90:182102, 2007.
- [6] K. H. Cho, K. H. Yeo, Y. Y. Yeoh, S. D. Suk, M. Li, J. M. Lee, M.-S. Kim, D.-W. Kim, D. Park, B. H. Hong, Y. C. Jung, and S. W. Hwang. Experimental evidence of ballistic transport in cylindrical gate-all-around twin silicon nanowire metal-oxide-semiconductor field-effect transistors. *Appl. Phys. Lett.*, 92:052102, 2008.

- [7] Yat Li, Fang Qian, Jie Xiang, and Charles M. Lieber. Nanowire electronic and optoelectronic devices. *Materials Today*, 9(10):18, 2006.
- [8] C. Thelander, P. Agarwal, S. Brongersma, J. Eymery, L.F. Feiner, A. Forchel, M. Scheffler, W. Riess, B.J. Ohlsson, U. Gösele, and L. Samuelson. Nanowire-based one-dimensional electronics. *Materials Today*, 9(10):28, 2006.
- [9] M.T. Bjork, B.J. Ohlsson, C. Thelander, A.I. Persson, K. Deppert, L.R. Wallenberg, and L. Samuelson. Nanowire resonant tunneling diodes. *Appl. Phys. Lett.*, 81:4458, 2002.
- [10] Jakob Wensorra, Klaus Michael Indlekofer, Mihail Ion Lepsa, Arno Forster, and Hans Lüth. Resonant tunneling in nanocolumns improved by quantum collimation. *Nano Lett.*, 5:2470, 2005.
- [11] Fang Qian, Yat Li, Silvija Gradec Caronak, Hong-Gyu Park, Yajie Dong, Yong Ding, Zhong Lin Wang, and Charles M. Lieber. Multi-quantum-well nanowire heterostructures for wavelength-controlled lasers. *Nature Mater.*, 7:701, 2008.
- [12] Mark S. Gudiksen, Lincoln J. Lauhon, Jianfang Wang, David C. Smith, and Charles M. Lieber. Growth of nanowire superlattice structures for nanoscale photonics and electronics. *Nature*, 415:617, 2002.
- [13] D. Vasileska, D. Mamaluy, H. R. Khan, K. Ravela, and S. M. Goodnick. Semiconductor Device Modeling. *J. Comput. Theor. Nanosci.*, 5:999, 2008.
- [14] J. H. Bardarson, I. Magnusdottir, G. Gudmundsdottir, C. S. Tang, A. Manolescu, and V. Gudmundsson. Coherent electronic transport in a multimode quantum channel with gaussian-type scatterers. *Phys. Rev. B*, 70:245308, 2004.
- [15] V. Gudmundsson, Y.-Y. Lin, C. S. Tang, V. Moldoveanu, J. H. Bardarson, and A. Manolescu. Transport through a quantum ring, dot, and barrier embedded in a nanowire in magnetic field. *Phys. Rev. B*, 71:235302, 2005.
- [16] E. P. Wigner and L. Eisenbud. Higher angular momenta and long range interaction in resonance reactions. *Phys. Rev.*, 72:29, 1947.
- [17] L. Smrčka. R-matrix and the coherent transport in mesoscopic systems. *Superlatt. and Microstruct.*, 8:221, 1990.
- [18] U. Wulf, J. Kučera, P. N. Racec, and E. Sigmund. Transport through quantum systems in the R-matrix formalism. *Phys. Rev. B*, 58:16209, 1998.
- [19] J. Behrndt, H. Neidhardt, E. R. Racec, P. N. Racec, and U. Wulf. On Eisenbud's and Wigner's R-matrix: A general approach. *J. Differ. Equ.*, 244:2545, 2008.
- [20] P. N. Racec, E. R. Racec, and H. Neidhardt. Evanescent channels and scattering in cylindrical nanowire heterostructures. *Phys. Rev. B*, 79:155305, 2009.

- [21] E. R. Racec, U. Wulf, and P. N. Racec. Fano regime of transport through open quantum dots. *Phys. Rev. B*, 82:085313, 2010.
- [22] Xavier Antoine, Anton Arnold, Christophe Besse, Matthias Ehrhardt, and Achim Schädle. A review of transparent and artificial boundary conditions techniques for linear and nonlinear Schrödinger equations. *Commun. Comput. Phys.*, 4:729, 2008.
- [23] J. R. Shewchuk. What is a good linear element? interpolation, conditioning, and quality measures. *Eleventh International Meshing Roundtable (Ithaca, New York), Sandia National Laboratories*, pages 115–126, 2002.
- [24] T. Koprucki, R. Eymard, and J. Fuhrmann. Convergence of a finite volume scheme to the eigenvalues of a Schrödinger operator. Preprint 1260, WIAS, Berlin, 2007.
- [25] Walter A. Harrison. *Applied Quantum Mechanics*. World Scientific, Singapore, 2000.
- [26] Triangle - A Two-Dimensional Quality Mesh Generator and Delaunay Triangulator, 2011. <http://www.cs.cmu.edu/~quake/triangle.html>.
- [27] TetGen - A Quality Tetrahedral Mesh Generator and a 3D Delaunay Triangulator, 2011. <http://tetgen.berlios.de/>.
- [28] P. Daly. An alternative high-order finite element formulation for cylindrical field problems. *I. J. Num. Meth. Eng.*, 19:1063, 1983.
- [29] P. Daly. Improved convergence rates for finite-element approximations in cylindrical coordinate geometries. *COMPEL*, 2:85, 1983.
- [30] Ivo Babuska. The finite element method with penalty. *Math. Comp.*, 27:221, 1973.
- [31] Arpack software, 2012. <http://www.caam.rice.edu/software/ARPACK/>.
- [32] Olaf Schenk and Klaus Gärtner. Solving unsymmetric sparse systems of linear equations with PARDISO. *Future Generation Computer Systems*, 20:475 – 487, 2004.
- [33] Olaf Schenk and Klaus Gärtner. On fast factorization pivoting methods for sparse symmetric indefinite systems. *Elec. Trans. Numer. Anal.*, 23:158–179, 2006.
- [34] PARDISO - sparse direct solver, 2012. <http://www.pardiso-project.org/>.
- [35] H. R. Schwarz. *Methoden der finiten Elemente*. Teubner, Stuttgart, 1980.
- [36] Larry J. Segerlind. *Applied Finite Element Analysis*. John Wiley & Sons, New York, 1984.